ERASMUS MUNDUS MASTER OF MECHANICAL ENGINEERING

MEMOIRE - THESIS

RAFAEL ADRIANO KUCHE SANCHES

THE USE OF CFD FOR INVESTIGATING FLUIDELASTIC INSTABILITY IN TUBE ARRAYS

June 2007

INSTITUT NATIONAL DES SCIENCES APPLIQUEES DE LYON - FRANCE
SCOLA TECHNICA SUPERIOR D'ENGINYERIA INDUSTRIAL DE BARCELONA DE LA UNIVERSITAT POLITECNICA DE CATALUNYA - ESPAGNE
THE COLLEGE OF THE HOLY AND UNDIVIDED TRINITY OF QUEEN ELIZABETH NEAR DUBLIN - IRLANDE

Abstract

There are several applications of tube arrays subject to cross flow in the industry, mostly for heat exchanging. These tubes are subject to forces arising due to the flow, and under certain conditions they can experience large amplitude self exited vibration, phenomenon named Fluidelastic Instability (FEI), a potentially catastrophic phenomenon when occurring in structures dimensioned for static loads. Through this work a brief review of the different methods of modelling FEI is presented, and the use of the commercial Computational Fluid Dynamics (CFD) solver FLUENT to predict the forces acting in a tube of an array subject to cross flow is analyzed. A few experiments are performed in order to compare the simulation results to real data. Finally, the Reynolds Stress Model (RSM) is found to provide better results, but still not very faithful to the reality. Guidelines for preparation of a good simulation of flow through a tube array, mesh construction and turbulent models are presented. A comparison between results from several turbulent models is presented. The most appropriate model is then chosen and more results are presented. Future work is pointed to simulation with dynamic mesh and to a methodology of adaptation of CFD results for quasi steady fluidelastic instability model.

Acknowledgements

I am very grateful to the European Commission for allowing me the opportunity of participating to the Erasmus Mundus program with a scholarship that made these two years possible.

Thanks to Professor Craig Meskell for introducing me to an exciting field despite complex. Thanks to Professor Boyer and all other staff that were very helpful during these two years.

I thank my colleagues for their companionship, helpfulness and for the moments of amusement we had, making this two years enjoyable.

I thank my family and friends in Brazil for not being so angry at me for the times that I've lost contact with them, they know I had my head full sometimes.

Table of Contents

List of Illustrations and Tables

List of Abreviations

CFD Computational Fluid Dynamics;

FEI Fluidelastic Instability;

FIV Flow Induced Vibration;

k-ε Turbulent model based on solving kinetic energy (k) and dissipation rate (ε);

k-ω Turbulent model based on solving kinetic energy (k) and specific dissipation rate (ω);

rk-ε Realizable k-ε, turbulent model improved from k-ε;

RNG Renormalization Group theory;

RSM Reynolds Stress Model turbulence model;

S-A Spalart-Allmaras turbulence model;

SST Shear-Stress Transport;

TCD Trinity College Dublin;

List of Symbols

A_D	Cross dragging area of a body;
A_L	Cross lifting area of a body;
C_{D0}	Drag coefficient at zero position;
C_L	Lift coefficient;
D	Diameter of the tube;
F_y	Fluidelastic force in y-direction;
F_D	Drag force;
F_L	Lift force;
f	Empirical friction factor;
k	Kinetic energy;
k_P	Turbulence kinetic energy at point;
L	Length of the tube;
N	Number of rows;
P	Pitch of the tube array;
P/D	Pitch ratio;
p	Static pressure;
$\overline{p}$	Average pressure;
p'	Fluctuating pressure;
U_0	Inlet velocity;
U_g	Gap velocity;
u_τ	Shear velocity;
$\overline{v}$	Average velocity;
v'	Fluctuating velocity;

y Position of the principal tube in y-direction

y_c Distance from the wall to the centre of a cell;

y^+ Wall unit;

y^* Wall unit;

y_P Distance from point to the wall;

$\dot{y}$ Acceleration of principal tube in y-direction;

Δp Pressure drop;

ε Dissipation rate;

μ Dynamic viscosity of the fluid;

ρ Fluid's specific mass;

θ Angle of a point at the surface of the tube;

ω Specific dissipation rate;

χ Empirical factor.

Chapter 1 - Introduction

When a flow interacts with a body or structure that presents resistance to the flow, this flow is forced by the structure to change its natural path and the fluid reacts by forcing back the structure, possibly causing displacement or deformation. If this force is not steady (could be periodic), vibration might be induced, this phenomenon is known as **Flow Induced Vibration** (FIV).

1.1 Where does it occurs

The phenomenon of FIV can be observed in bridges and towers subject to wind, airplanes at high speed, cross flow heat exchangers, but it also occurs in smaller scale in pipe lines, valves and other flow control instruments. When vibrations occur in structures designed to be static, the structure can be overloaded and a disastrous failure can happen. There are some famous cases in history, such as the 1940 Tacoma Narrows Bridge collapse in Washington[1], in that case was the wind that provoked FIV.

Industry and Power Plants make use of tube bundles subject to cross flow for important functions, usually involving heat transfer between two fluids, in equipments such as steam generators, condensers, etc. FIV commonly happens in tube arrays and can also cause to fail, for example, the steam generator of a power plant by shortening the life of structural components due to fatigue and wear caused by friction and constant impacting. The cost in power production during repairs added to the cost of repair itself would be considerably important. Therefore, it is very important to predict the behaviour of a tube array and the parameters (especially the velocity) at which FIV would occur.

1.2 The needs

For designers, there is a paradox when projecting structures that will be eventually subject to cross flow. To avoid FIV, the structure should be stiff and heavy, but this will make it expensive due to the amount of material required. In cross flow heat exchangers the case is even more complex: in order to achieve a good rate of heat transfer, tubes with low thermal resistance and consequently thin walled with low stiffness are required, but to resist vibration the tubes should be stiff (thick walled), another important parameter for heat exchange is the velocity of flow, an increased velocity increases heat exchange, but also increases the flow energy and its reaction forces. To avoid FIV problems in designed tube arrays subject to cross flow, the critical flow velocity at which it occurs must be predicted through a reliable model.

1.3 The aims

In the present work, the causes of FIV are briefly reviewed and some models are commented. Specifically, the mechanism of **Fluidelastic Instability** (FEI) for producing FIV received special attention.

The present work intends to study the use of **Computational Fluid Dynamics** (CFD) to simulate and study the flow in a tube bundle and get relevant data to predict FEI is analyzed through comparison between the computational results and those from some experiments realized. The computational simulations are made by using the commercial CFD package FLUENT. Many relevant considerations for defining a good simulation method are commented, such as which viscous turbulent model that provides better results and the mesh design. Compare between results of distinct turbulent models is also an objective

Chapter 2 - Literature Review

With the development of research in FIV field, there were identified three mechanisms that cause FIV. These mechanisms where first defined by Paidoussis[2] and have been widely accepted, they are explained by Zukauskas[3] and are currently described by as:

1. **Turbulent buffeting**: forces arising due to turbulent fluctuations of flow pressure;

2. **Flow periodicity**: forces due to formation of vortex streets in the tube wakes and also acoustic resonance;

3. **Fluidelastic Instability (FEI)**: forces arising when the tubes move out of their equilibrium position in the bundle and their Fluidelastic interaction with the flow.

Studies about cases 1 and 2 have provided good models that can predict accurately the behaviour of a tube array subject to cross flow. However, the 3rd case is actually the most complex and for purpose of study is usually sub-classified into two categories:

- **Stiffness controlled**: requires all or several tubes in a bundle to be flexible (multi degrees of freedom);

- **Damping controlled**: occurs when only one flexible tube is inserted into a rigid tube bundle, the flow acts as a negative damper, supplying energy to the vibrating tube instead of dissipating energy (single degree of freedom).

The Fluidelastic instability was firstly pointed by Roberts[4] and later Connors[5] advanced and defined models and equations to predict what is now known as stiffness controlled mechanism, but his model did not apply to the damping controlled case. Later on, Price[6] investigated the use of Connors equation and compared it to other new methods.

However, the damping controlled Fluidelastic instability still not have an accurate model and much effort has been made by researchers to develop one, many complex analysis have been made, such as Meskell[7], that considers the vortex convection to represent the transient nature of the Fluidelastic forces in a tube array. A comparison between these mechanisms was made by Paidoussis and Price[8], underlying the equations for the acting forces with their physical interpretation.

Usually, Fluidelastic instability does not occurs itself alone, but associated to one of the previous mechanisms (turbulence or vortex shedding), that will firstly displace the tube through low amplitude vibrations, then the tube starts to interact with the flow and the FEI begins.

2.1 Modelling methods

The models which have been created to solve or predict the FEI cases can be basically separated by their nature as: empirical, semi-empirical, or purely theoretical, but even the so called theoretical models assume known some parameters that must be empirically obtained.

The empirical models, as the name suggests, measure all fluid and flow parameters directly, therefore they require well controlled experiments and complex data analysis techniques. This renders these models expensive and impracticable for most situations.

Price and Paidoussis[9] proposed the quasi-steady semi-empirical model which requires only limited empirical data. This approach has been detailed and modified by Paidoussis and Price[8] and later was modified and improved by Granger and Paidoussis[10], but still depend on experimental data.

The basic idea behind the quasi-steady model is that the flow forces acting on a tube in movement can be approached at each position of its trajectory by the force acting on a tube statically displaced to that position. From this idea and considering the case of only one flexible tube in a rigid tube array with only one degree of freedom to vibrate in the *y*-direction, transversely to the *x*-direction of the flow (Figure 3.1), the basic equation for the fluidelastic force in the vibration direction (F_y) presented by Paidoussis and Price is presented:

$$F_y = \frac{\rho U^2}{2} LD\left[\frac{\partial C_L}{\partial y} y - C_{D_0} \frac{\dot{y}}{U_g}\right] \tag{2.1}$$

Where ρ is the fluid specific mass, U_g is the gap velocity, L and D are the length and the diameter of the tube, C_L is the lift coefficient, C_{D0} is the drag coefficient at zero position and $\dot{y}$ is the acceleration in y-direction.

The most recent models for damping controlled vibration are usually improvements of equation (2.1), adding terms to represent the delay between tube displacement and the fluid-dynamic forces generated thereby and/or other features. However, the drag coefficient and gradient of lift coefficient still must be obtained from empirical data. In an age where computer simulations are used extensively in all fields of science, and with the development and improvement of CFD techniques, the use of computer to quickly and inexpensively obtain data to use in FIV predictions is a very attractive idea. The use of the commercial CFD package FLUENT for obtaining fluid force coefficients has already been presented by Meskell[11], but no suitable comparison between experimental results and the computational results have been made. In this work a few experiments are realized and the results are minutely compared.

2.2 Fluid-dynamic forces

It is well known that the forces generated by a flow over a body can be due to viscosity effects (skin friction) and due to the pressure field generated according to the form of the body and the flow characteristics (e. g. lift in an airfoil). For purposes of study, the theory of aerodynamics decomposes these forces into **Drag**, acting in the direction of the flow, and **Lift**, acting transversally to the flow direction. These forces of lift (F_L) and drag (F_D) are usually expressed by the following equations (2.2) and (2.3):

$$F_D = \frac{C_D \rho U^2}{2} A_D \tag{2.2}$$

$$F_L = \frac{C_L \rho U^2}{2} A_L \tag{2.3}$$

where C_L and C_D are drag and lift coefficients dependent basically on the body shape, and A_L and A_D are respectively the cross lifting and dragging areas of the body.

For cross flow of gases (low viscosity) through tube banks, there is a significant pressure drop as the fluid passes through the rows, so that the parcel of the aerodynamic force due to viscosity is very small comparing to the parcel due to the pressure profile (less then 10% overall). Therefore, for the study of forces in tube arrays, it is much more relevant the study of forces generated from the pressure around the tubes.

In Graphs 2.1 can be observed an illustration for the pressure profile around a cylinder, which shows results obtained in one of the simulations of this work for one tube displaced in direction transverse to the flow at 5% of its diameter in a normal triangular tube array. Graphs 2.1 are also important because it also introduces a form of presenting results that is very often

used in this work, showing the convention adopted for the angle in relation to the flow direction.

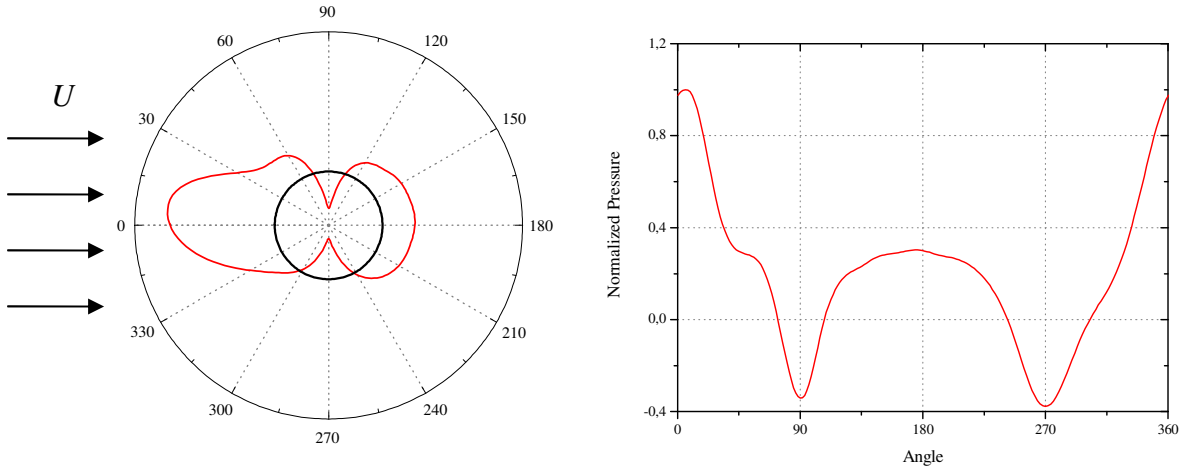

(a) **(b)**

Graphs 2.1 Static pressure profile over a tube displaced of 2 [mm] in a staggered normal triangular array **(a)** cylindrical representation and flow direction representation; **(b)** Cartesian representation for the same profile.

A significant pressure drop can be observed between the front and the back of the tube, this will basically define the drag force acting on the tube. Similarly to the drag, the lift will be defined by the pressure acting in the top and bottom of the cylinder.

Therefore, by knowing the pressure around a cylinder, these forces due to the pressure can be calculated by integrating the profile through equations (2.4) and (2.5) following:

$$F_D = \frac{DL}{2}\int_0^{2\pi}(\cos\ \theta)\,d\,\theta \tag{2.4}$$

$$F_L = \frac{DL}{2}\int_0^{2\pi} p(-\sin\theta)d\theta \tag{2.5}$$

where p is the static pressure and θ the angle.

By doing a CFD simulation, the pressure profile $p(\theta)$ around a tube is obtained, and hence the forces of drag and lift are easily calculated by employing equations (2.4) and (2.5). Knowing forces, the coefficients of drag and lift can be calculated through equations (2.2) and (2.3), these coefficients, on the other hand, can be used at FEI evaluation models.

Chapter 3 - Methods and Objectives

As referred in section 2.1 previously, mostly all the existent models for FEI depend on empirical data (e.g. force coefficients) and the realization of experiments for all the possible configurations of arrays and various ranges of velocities is not an attracting option for every time that a FIV analysis has to be done. Hence is desirable an alternative way to obtain this data. CFD is an interesting alternative as commented previously.

The main objective of this work is to find a reliable simulation model to obtain the necessary data for prediction of FEI in tube arrays. To achieve this objective, the methodology applied is:

- **Computer simulations (CFD)**: two dimensional (2-D) simulations are made using resources provided by FLUENT, obtaining results for different models available;

- **Experiments**: a model of tube arrays similar to that of the simulations is tested in wind tunnel and the pressure profile is measured for a cross section of a tube of interest;

- **Comparing and improving**: the results from the simulations are then compared to those of the experiments, and so the better simulation model can be found and improved to the best possible fit to the experimental results.

An assumption for this work that is very important to emphasize is that, as the quasi-steady model is followed, all the computer simulations and experiments are realized as if they were in steady state.

3.1 The case under study

There are lots of different possible configurations of tube arrays actually used by the industry, but it is necessary to fix some parameters in order to start a study. In this case, the geometry chosen to start the analysis is shown in Figure 3.1, and has the following characteristics:

This specific geometry was chosen because it has already been in use by researchers at the Laboratory of Fluid Mechanics at Trinity College Dublin (TCD).

- Normal triangular staggered array;
- 5 rows;
- Pitch ratio P/D = 1.32;
- Tube diameter D≈40 [mm];
- Working Fluid: air at normal conditions of temperature and pressure;

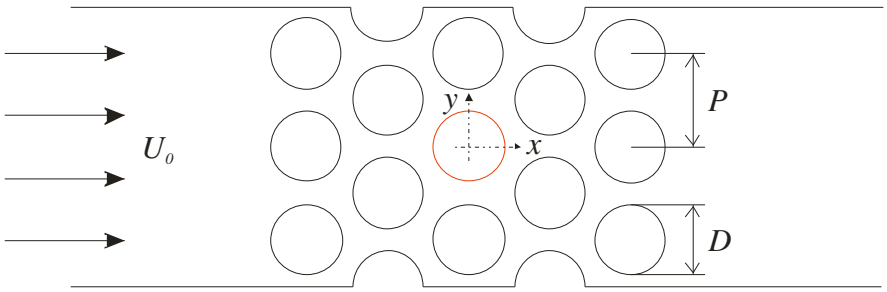

Figure 3.1 Scheme of the case under study

The tube shown in red, in the middle of the third row in Figure 3.1, is the principal tube, representing a flexible tube which has one degree of freedom to move on the y-direction (transversal to the flow direction), while all other tubes are rigid (static). That tube will be

displaced in y-direction and the pressure profile will be measured during the experiment or calculated by simulation. The tube in that position was chosen because represents a tube immerse in an array and expresses a general situation.

- **Tested velocities**: U_0 = 5 and 8.8 [m/s];
- **Positions of the main tube**: y between 0 and 6 [mm].

The maximum test velocity could not exceed 8.8 m/s, this was the maximum possible to be obtained due to the limitation of the wind tunnel's engine power.

Chapter 4 - Experimentation

As was referred in section 2.1, there is a necessity of comparing the pressure profiles obtained by simulation with real experimental data. So, using the installations and equipment available in Laboratory of Fluid Mechanics in the Department of Mechanical and Manufacturing Engineering at Trinity College Dublin, some experiments have been performed.

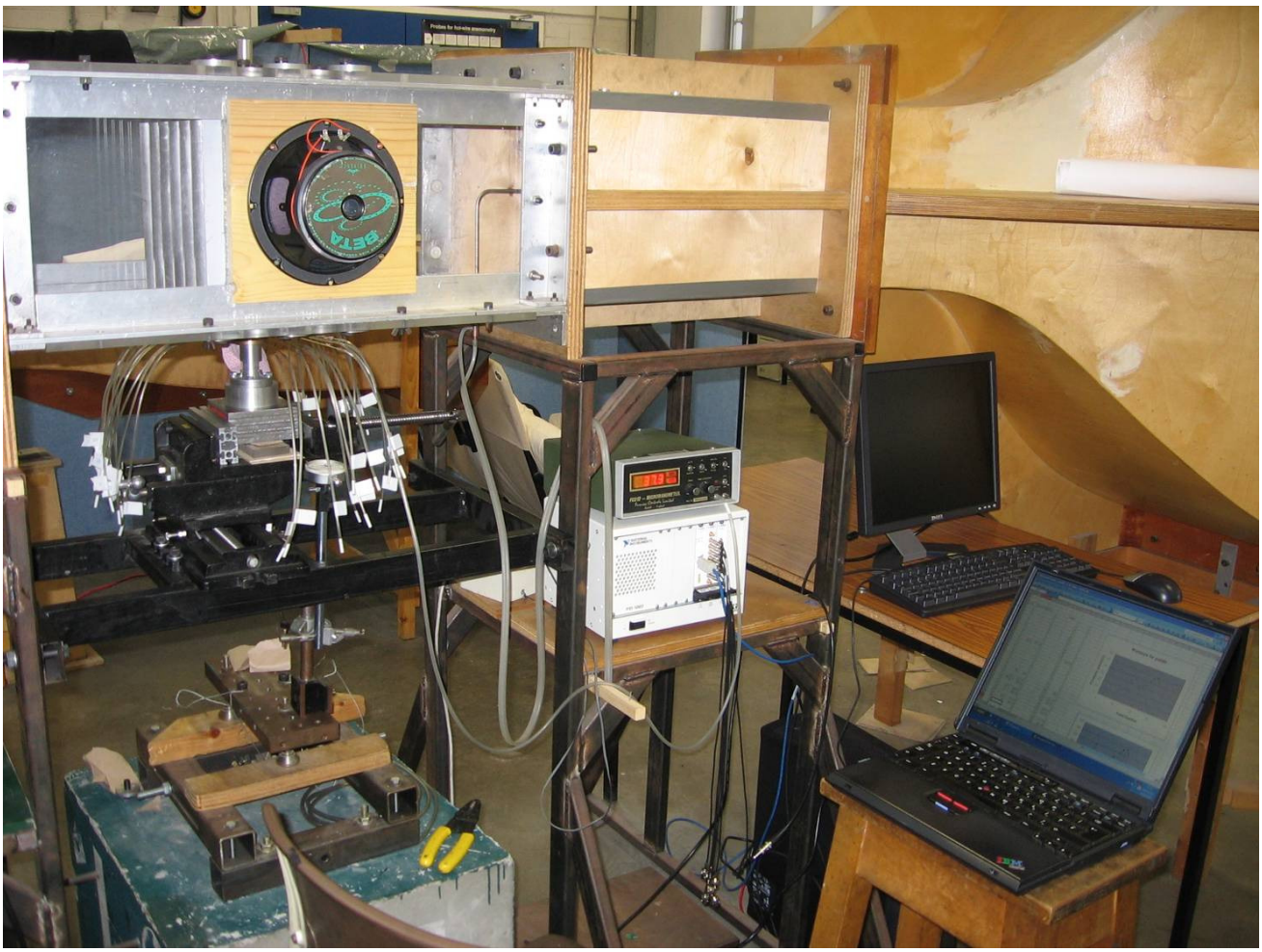

Figure 4.1 Overview of the experiment and instrumentation utilized

An overview of the experiment running showing the experiment utilized can be observed in Figure 4.1. Note that the speakers installed in the region of the arrays where not

part of this experiment, they where actually being used by another student using the same wind tunnel for his experiment.

4.1 Instrumentation

Details on the necessary equipment that can be seen in Figure 4.1 follow:

- **Wind tunnel**: drawdown, test section of 300x300 [mm];
- **Digital manometer**: Furness, resolution of 0.1 [mmH_2O];
- **Positioning system**: Rigid base allowing x and y displacing (Figure A1.3);
- **Calliper**: high precision, used to measure the displacement;
- **Main tube**: prepared with 36 circumferentially equispaced tappings (Figure 4.2).

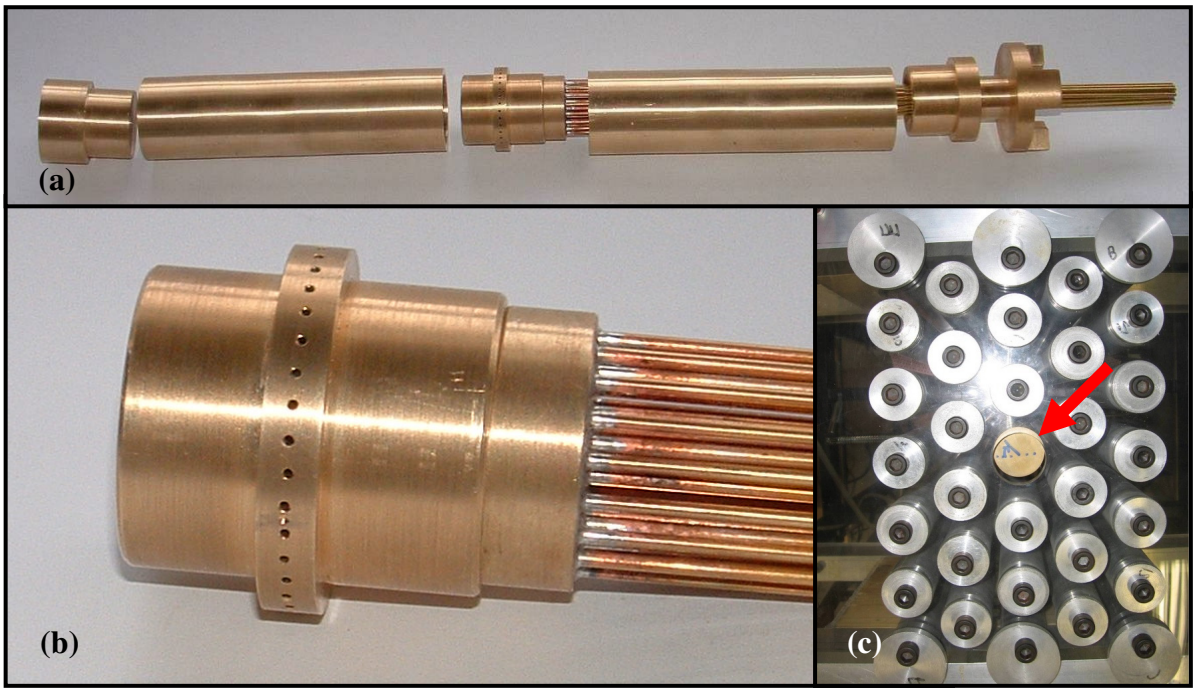

Figure 4.2 (a) components of the main cylinder semi-assembled; **(b)** central component which contains the pressure tappings; **(c)** main tube assembled in the middle of the array (notice the vertical displacement).

Figures 4.2 (a) and (b) shows the equipment that is certainly the most important for this experiment, the main tube was manufactured in brass by a technician in the manufacturing facilities of the Department of Mechanical and Manufacturing Engineering. Figure 4.2 (c) also shows the configuration of the main cylinder assembled into the tube array and displaced for experimentation. Details on the main tube and a sketch of the wind tunnel can be seen on Appendix 1.

4.2 Experimental proceedings

Firstly, the 36 Tappings were numerated in sequential order relative to an ordinarily chosen 1st tapping, by adding labels to their respective extension tubes. Then the main tube was assembled to the array and to the positioning base, attending to the vertical alignment and to the positioning at the centre of the array. At this moment it was not possible to know the exact angle of each tapping, but this could be later verified from the results.

With the assembly done, the experiment was started. Firstly, the velocity must be adjusted by setting up the aperture at the outlet of the wind tunnel. By closing the aperture, charge is added to the outlet, increasing the outlet pressure, thou decreasing the drop pressure between inlet and outlet, causing the flow velocity to decrease. The velocity is measured at inlet, just before the array, by using a digital micro-manometer connected to a Pitot tube, so that the velocity is automatically calculated by the instrument from the measured dynamic pressure. With the velocity controlled, a not so precise measurement of the pressure drop is made, just by inserting a hose connected to the manometer into a screw hole just after the array.

After all set-up and adjustments done, the measurement of the pressure profile begins. One by one; the hose id fitted to the extension tube and a reading can be performed. At the

velocity range of the experiment, the flow is turbulent, so that the pressure is not constant, but this study is looking for steady state, as was explained in section 3 previously, so what is going to be measured is the average pressure at each point. To do so, the manometer has a tool that permits adjusting the period during witch the average pressure is measured. When the period is set to be minimal, the pressure value is observed to oscillate a lot, as if it was a "real time" measurement of turbulent flow. By increasing the period, the instrument will average the measurements made during that period, and a mean or average pressure can be read.

The readings were input to the laptop and instantly plotted; hence if a value seems to break far away from the nearby values, it could be double checked. Finishing the profile, the tube is then displaced to a new position, the displacement is controlled using the calliper attached to the base.

So, the velocities tested were 5 and 8.8 [m/s], this was the maximum speed that was possible to obtain in the wind tunnel.

4.3 Experimental results and discussion

The measured pressure profiles are plotted separated by inflow velocity. The results for a same velocity are plotted together to facilitate the perception of the modification of the profile with the displacement and so the understanding of the comments next. The data obtained from the experiments can be consulted on Tables A2.1 and A2.2 on Appendix 2.

The first profile to be measured was for the position 0 [mm] at the velocity of 8.8 [m/s], shown in Graphs 4.2 (black line), and so all the possible mistakes were probably made while the operator was getting used to the equipment. Even so, some interesting points can be

sharpen, as the sudden increase on pressure at the back of the cylinder (180°) and those two symmetric peaks at around 50° and 310°, these increases in pressure could be due to the fact that in these regions there is a re-encounter and mixing of the flows coming from top and bottom of the cylinders. It is interesting that when breaking the symmetry; these peaks of pressure just disappear, and also they are not observed for the zero position at 5 [m/s], probably because the turbulence at this velocity is much lower.

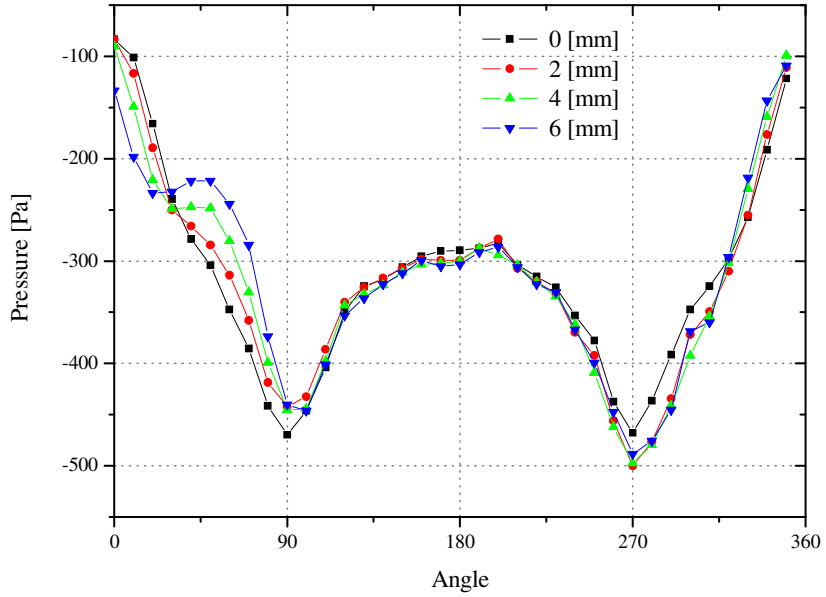

Graphs 4.1 Measured pressure profiles at U_0 = 5 [m/s]

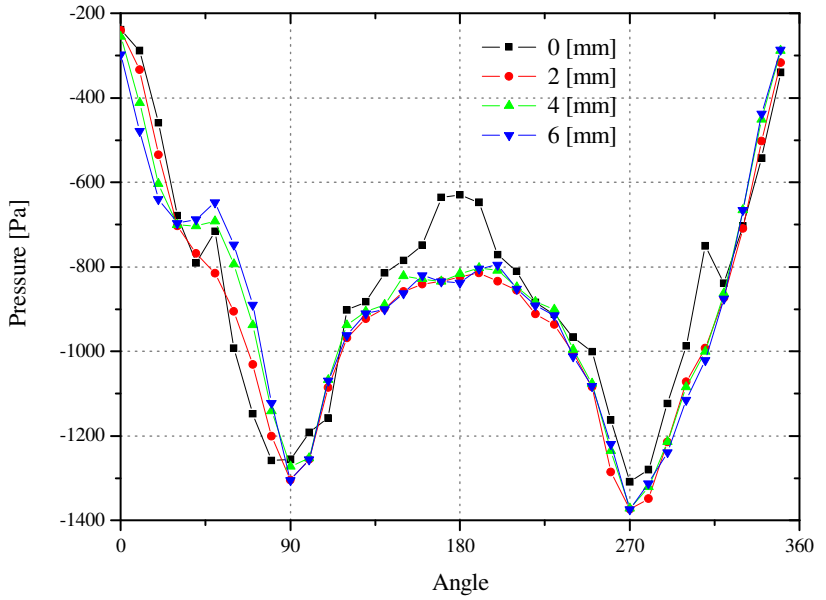

Graphs 4.2 Measured pressure profiles at U_0 = 8,8 [m/s]

Now, what happens when the tube is displaced? The changes in the profiles can be observed basically in three regions:

- between 30° and 60°, where a "shoulder" appears and increases as the displacement is increased, this is caused by an approximation of this tube to the tube in the row before, creating a blockage and inducing a lower velocity and consequently higher pressure;

- at the extreme top and bottom (90° and 270°), these are the gaps, and by the same principle, the displacement causes the velocity to decrease in the top (90°), causing an increase in pressure, while in the bottom (180°), the opposite occurs.

However at 8.8 [m/s] there seems to have an decrease in pressure both on top and bottom, but this is surely effect of any mistakes on the experiment, as can be observed, the pressures are higher both on top and on bottom.

To estimate the lift and drag from the experimental results, the equations (2.4) and (2.5) are adapted to a numerical integration by using the trapezoidal rule, forming equations (4.1) and (4.2):

$$F_D = \frac{D}{4}\sum_{i=1}^{n}(\theta_{i+1}-\theta_i)(p_i+p_{i+1})\cos\left(\theta_i+\frac{\theta_{i+1}-\theta_i}{2}\right) \tag{4.1}$$

$$F_L = \frac{D}{4}\sum_{i=1}^{n}(\theta_{i+1}-\theta_i)(p_i+p_{i+1})\left[-\sin\left(\theta_i+\frac{\theta_{i+1}-\theta_i}{2}\right)\right] \tag{4.2}$$

Observe that the length is not present to these equations because our analysis is two dimensional, so the forces calculated are in [N/m] and disposed in Table 4.1.

Table 4.1 Calculated drags and lifts from the experimental pressure profiles

y [mm]	U_0 = 5 [m/s]		U_0 = 8.8 [m/s]	
	F_D [N/m]	F_L [N/m]	F_D [N/m]	F_L [N/m]
0	3,06	-0,04	6,10	-0,40
2	3,07	-1,20	8,45	-2,62
4	3,36	-1,47	8,45	-3,53
6	3,41	-1,67	8,46	-3,93

From Table 4.1 some effects can be verified:

- The lift is opposite to the imposed displacement (negative values), that would cause a damping effect to any vibration;

- The lift at zero position was expected to be zero and this was verified despite the small residual from experimental error, and the error is observed to be bigger for 8.8 [m/s], but this would be expected for the reasons already explained about this specific case;

- The lift is significantly altered with the displacement for both velocities, while the drag does not change so drastically, truthfully there is practically no change at 8.8 [m/s] when disregarding the zero position.

Chapter 5 - Computer Simulations

In order to reduce the cost of studying FEI in tube arrays; the application of computer simulation is an attracting alternative to experimentation. For this study, the commercial CFD package FLUENT has been used.

FLUENT is one of the best known and respectable commercial CFD solvers available nowadays. This reputation; allied with several options and tools for pre-processing (meshing and defining the model) and post-processing (plotting and analyzing results), and regarding the fact that TCD and INSA had a number of licenses available, are the reasons that induced to its employment in this study.

5.1 The boundary conditions

The simulation conditions must be equivalent to the conditions used during the experimental procedures, however, the exact conditions at the experiment are not known, what is known is that the air enters the wind tunnel approximately at normal conditions of temperature and pressure, and because of the pressure gradient caused by the centrifugal ventilator (sketch in Appendix 1, Figure A1.1) the air is accelerated to a velocity that is measured before the tube array. This measured velocity U_0 is then used as inlet boundary condition. The outlet boundary condition is set to be zero, as it was not measured during the experiment and as it is known that for low velocity the air acts as an incompressible flow (ρ is constant). The side borders as well as the tubes are defined as standard walls. The extension to outlet measures 37 diameters to avoid that the outlet zero pressure condition exert influence over the flow in the tube array region. These configurations may be better visualised in Figure 5.1 that follows.

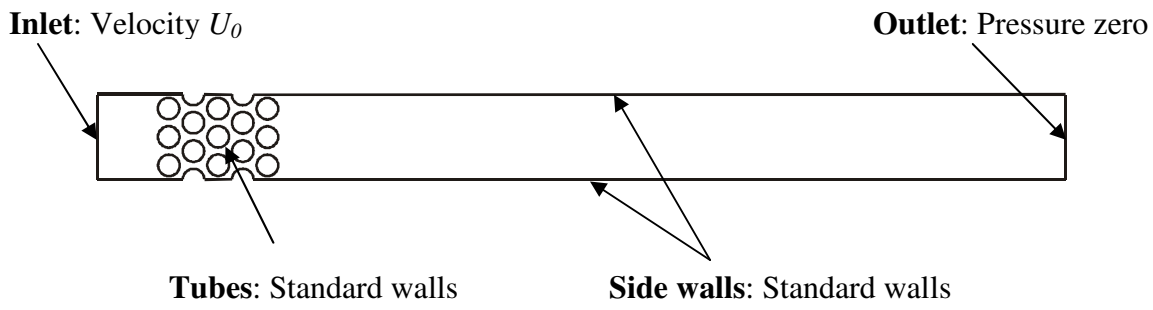

Figure 5.1 Setup of boundary conditions

5.2 Turbulent models

Turbulent flows are characterized by fluctuating velocity fields. These fluctuations mix transported quantities such as momentum, energy, and species concentration, and cause the transported quantities to fluctuate as well. When experimentally measuring a turbulent flow, one uses statistical parameters to express its characteristics, for example velocity and pressure are defined by an average value ($\overline{v}$ or $\overline{p}$) and a fluctuating value (v' or p'):

$$\begin{aligned} p &= \overline{p} + p' \\ v &= \overline{v} + v' \end{aligned} \tag{5.1}$$

Since these fluctuations can be of small scale and high frequency, they are too computationally expensive to simulate directly in practical engineering calculations. Instead, the instantaneous (exact) governing equations can be time-averaged, ensemble-averaged, or otherwise manipulated to remove the small scales, resulting in a modified set of equations that are computationally less expensive to solve. However, the modified equations contain additional unknown variables, and turbulence models are needed to determine these variables in terms of known quantities.

When working with turbulent flows, as are most of the applications of tube arrays; there are two possible solvers available in FLUENT, and they are:

- **Large Eddy Simulation** (LES): originally developed for atmospheric boundary layer simulations, that computes a time dependent simulation, and requires an unthinkable computational cost, being inadequate to the present work;

- **Reynolds Averaged Navier-Stokes** (RANS): presents transport equations only for the mean quantities of the flow, with all the scales of turbulence being modelled, this approach permits a solution for the mean flow variables greatly reducing the computational effort, much more interesting for this work.

However, these RANS equations introduce some new terms, the Reynolds stresses, which have to be modelled in order to give closure to the system. For this task, FLUENT has available the called **viscous models**, each one with some special options, but these models are all based in one of two models: the Boussinesq approach; or the Reynolds Stress Transport Model.[12] The Boussinesq approach is used by the models **Spalart-Almaras**, **k-ε** and **k-ω**, while the Reynolds Stress Transport Model is only called **RSM**. One fundamental difference between these models is that the Boussinesq approach considers that turbulent viscosity is the same in all directions (isotropic), while the RSM model does not, being certainly more realistic. Next are presented some descriptions of each turbulence model (based on FLUENT User's Guide[12]).

5.2.1 Spalart-Allmaras

The Spalart-Allmaras[13] model is a relatively simple one-equation model that solves a modelled transport equation for the kinematic eddy (turbulent) viscosity. This embodies a relatively new class of one-equation models in which it is not necessary to calculate a length scale related to the local shear layer thickness. The Spalart-Allmaras model was designed

specifically for aerospace applications involving wall-bounded flows and has been shown to give good results for boundary layers subjected to adverse pressure gradients.

In its original form, the Spalart-Allmaras model is effectively a low-Reynolds-number model, requiring the viscous-affected region of the boundary layer to be properly resolved. In FLUENT, however, the Spalart-Allmaras model has been implemented to use wall functions when the mesh resolution is not sufficiently fine. On a cautionary note, however, the Spalart-Allmaras model is still relatively new, and no claim is made regarding its suitability to all types of complex engineering flows.

5.2.2 The k-ε model and its variations

The simplest "complete models" of turbulence are two-equation models in which the solution of two separate transport equations allows the turbulent velocity and length scales to be independently determined. The standard k-ε model in FLUENT falls within this class of turbulence model and has become the workhorse of practical engineering flow calculations in the time since it was proposed by Launder and Spalding[14]. Robustness, economy, and reasonable accuracy for a wide range of turbulent flows explain its popularity in industrial flow and heat transfer simulations. It is a semi-empirical model, and the derivation of the model equations relies on phenomenological considerations and empiricism.

As the strengths and weaknesses of the standard k-ε model have become known, improvements have been made to the model to improve its performance. Two of these variants are available in FLUENT: the **RNG k-ε** model[15] and the **realizable k-ε** model[16]. The main differences between these models are described next.

- The standard k-ε model[14] is a semi-empirical model based on model transport equations for the turbulence kinetic energy (k) and its dissipation rate (ε). The model

transport equation for k is derived from the exact equation, while the model transport equation for ε was obtained using physical reasoning and bears little resemblance to its mathematically exact counterpart. The standard k-ε model is therefore valid only for fully turbulent flows.

- The RNG k-ε model was derived using a rigorous statistical technique (called renormalization group theory[17]). It is similar in form to the standard k-ε model, but includes some refinements that make it more accurate and reliable for a wider class of flows than the standard k-ε model.

- The realizable k-ε model[16] is a relatively recent development and differs from the standard k-ε model by having a new formulation for the turbulent viscosity and a new transport equation for the dissipation rate, ε, has been derived from an exact equation for the transport of the mean-square vorticity fluctuation. The term "realizable" means that the model satisfies certain mathematical constraints on the Reynolds stresses, consistent with the physics of turbulent flows. An immediate benefit of the realizable k-ε model is that it more accurately predicts the spreading rate of both planar and round jets. It is also likely to provide superior performance for flows involving rotation, boundary layers under strong adverse pressure gradients, separation, and recirculation.

5.2.3 The standard k-ω and SST k-ω models

The standard k-ω model in FLUENT is based on the Wilcox k-ω model[18], which incorporates modifications for low-Reynolds-number effects, compressibility, and shear flow spreading. The Wilcox model predicts free shear flow spreading rates that are in close agreement with measurements for far wakes, mixing layers, and plane, round, and radial jets,

and is thus applicable to wall-bounded flows and free shear flows. The standard k-ω model is an empirical model based on model transport equations for the turbulence kinetic energy (k) and the specific dissipation rate (ω), which can also be thought of as the ratio of ε to k.

The shear-stress transport (SST) k-ω model is similar to the standard k-ω model including some refinements. It was developed by Menter[19] to effectively blend the robust and accurate formulation of the k-ω model in the near-wall region with the free-stream independence of the k-ε model in the far field. To achieve this, the k-ε model is converted into a k-ω formulation.

These features make the SST k-ω model more accurate and reliable for a wider class of flows (e.g., adverse pressure gradient flows, airfoils, transonic shock waves) than the standard k-ω model. Other modifications include the addition of a cross-diffusion term in the ω equation and a blending function to ensure that the model equations behave appropriately in both the near-wall and far-field zones.

5.2.4 RSM model

The Reynolds stress model (RSM)[20, 21, 22] is the most elaborate turbulence model that FLUENT provides. Abandoning the isotropic eddy-viscosity hypothesis, the RSM closes the Reynolds-averaged Navier-Stokes equations by solving transport equations for the Reynolds stresses, together with an equation for the dissipation rate. This means that five additional transport equations are required in 2D flows and seven additional transport equations must be solved in 3D.

Since the RSM accounts for the effects of streamline curvature, swirl, rotation, and rapid changes in strain rate in a more rigorous manner than one-equation and two-equation models, it has greater potential to give accurate predictions for complex flows. However, the fidelity

of RSM predictions is still limited by the closure assumptions employed to model various terms in the exact transport equations for the Reynolds stresses. The modelling of the pressure-strain and dissipation-rate terms is particularly challenging, and often considered to be responsible for compromising the accuracy of RSM predictions.

The RSM might not always yield results that are clearly superior to the simpler models in all classes of flows to warrant the additional computational expense. However, use of the RSM is a must when the flow features of interest are the result of anisotropy in the Reynolds stresses.

5.2.5 Comparison of computational cost

In terms of computation, the Spalart-Allmaras model is the least expensive turbulence model of the options provided in FLUENT, since only one turbulence transport equation is solved.

As the number of equations of a model increases and extra terms are added, the CPU time increases. Following this rule, the standard k-ε model clearly requires more computational effort than the Spalart-Allmaras; computations with the RNG k-ε model tend to take 10-15% more CPU time than with the standard k-ε model. Like the k-ε models, the k-ω models are also two-equation models, and thus require about the same computational effort. Due to the increased number of the transport equations for Reynolds stresses, on average, the RSM in FLUENT requires 50-60% more CPU time per iteration compared to the k-ε and k-ω models. Furthermore, 15-20% more memory is needed.

Aside from the time per iteration, the choice of turbulence model can affect the ability of FLUENT to obtain a converged solution. For example, the RNG model is more likely to be susceptible to instability in steady-state solutions than the k-ε. Similarly, the RSM may take

more iterations to converge than the k-ε and k-ω models due to the strong coupling between the Reynolds stresses and the mean flow.

5.3 The mesh

The generation of the mesh has shown itself to be as important as the selection of the viscous model for simulation. The mesh was modelled by using the software GAMBIT (part of the FLUENT package). Some people would say that conceiving a mesh is almost an art, it involves many technical issues and mainly know-how.

A mesh is usually characterized by these features: cell geometry: could be basically triangular or quadratic; organization: if the cells follow any pattern or they are unstructured; cell size: if coarse or refined; boundary layer: usually the near wall receives special attentio; cell shape: skewness.

During the realization of this work, several meshes were conceived, differing in size, cell organization, cell size and cell geometry. The mesh is basically separated in 3 regions: a small inlet, the tube bundle, and the outlet channel (made big for a reason).

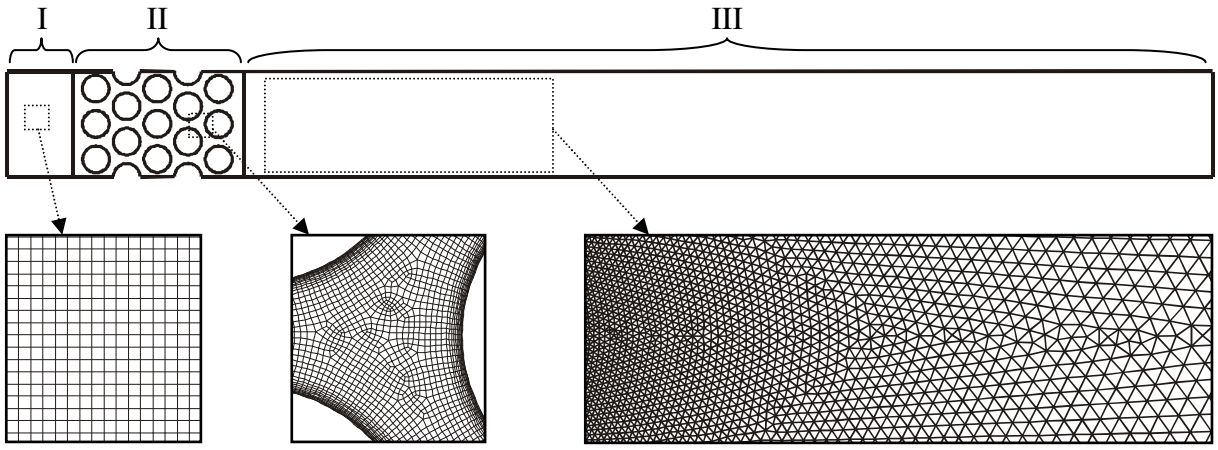

Figure 5.2 The three regions of meshing and their respective mesh layouts

I. **The inlet**: does not need very precise results, quadratic cells of 2x2 [mm] were used in this region.

II. **The tube array**: The boundary layer was made extremely thin to meet the near wall mesh guidelines. The cells were quadratic unstructured sizing around 0.6x0.6 [mm] out of the boundary layer.

III. **The outflow region**: measures more than 30D as previously explained, the mesh is composed of non structured triangular cells with size increasing at a constant ratio as they get far from the tube array in order to lower the computational cost for calculations (no need for refined mesh, as the geometry is simple and easy to be simulated).

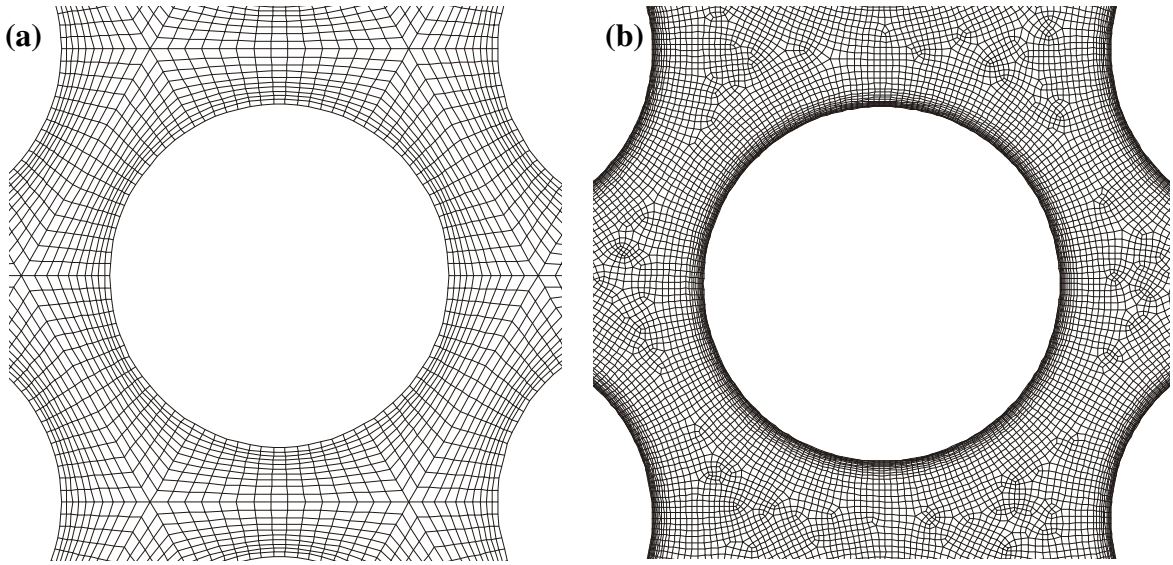

Figure 5.3 Mesh types **(a)** in hexagonal blocks; **(b)** unstructured with extra thin mesh at cylinder wall.

The tube array (region II) is the most important and deserves special attention for meshing. The first mesh was designed taking profit on the symmetric pattern of the tube array, as shown in Figure 5.3(a), by modelling hexagonal blocks around each cylinder, and the blocks were composed of quadratic cells formed in polar orientation around the cylinder, with

their heigh increasing gradually as they get far from the tube. This structure would permit one block to be modified independently from the others. This would be very useful in case of using a dynamic mesh for a unsteady (time dependent) simulation, as made by Schroder and Gelbe[23].

As the present work stays in steady state, there was no need to keep using the hexagonal blocks. The main reason that induced the withdraw of the structured mesh was the fact that when meshing for a displaced tube, the mesh would get deformed, very thin in the displacement direction and coarse in the opposite direction, another limitation is that a displacement of 6 [mm] would not be possible because the tube would touch the hexagon's border. The geometry of mesh used for the latest simulations was like the one shown in Figure 5.3(b), composed of a very refined boundary layer around the tubes and a thin unstructured quadratic mesh in the tubes region.

5.3.1 Meshing near wall region

The pressure at the wall significantly affects a turbulent flow, so special attention should be paid to develop a good simulation. The RANS solvers use special models based on semi-empirical formulas or functions to calculate the near wall flow. FLUENT has basically four options of near wall region modelling:

- **Standard wall function**: contained by default in every turbulent model;
- **Non-Equilibrium Wall Functions**: is available as an optional with the following viscous models: k-ε and RSM;
- **Enhanced wall treatment**: is available as an optional with the following viscous models: k-ε and RSM;

- **Enhanced wall functions**: are available with the following viscous models: Spalart-Allmaras, k-ω and LES.

FLUENT offers the user another option of creating personalized wall functions. Each one of these models requires determined mesh conditions to provide good results. Basically two parameters are used for verifying the mesh quality: the wall units y^* and y^+, these are parameters calculated for cells adjacent to the wall to define which model will be used to calculate that region, they are defined by equations (5.2) and (5.3) as:

$$y^+ \equiv \frac{\rho u_\tau y_c}{\mu} \tag{5.2}$$

$$y^* \equiv \frac{\rho C_\mu^{1/4} k_P^{1/2} y_P}{\mu} \tag{5.3}$$

where u_τ is the shear velocity, y_c is the distance from the wall to the centre of the cell, μ is the dynamic viscosity of the fluid, k_P is the turbulence kinetic energy at point P, y_P is the distance from point P to the wall.

FLUENT has different requirements of y^+ for different options of near wall modelling. Starting for standard wall functions, these are the guidelines:

- For standard or non-equilibrium wall functions, each wall-adjacent cell's centroid should be located within the log-law layer, $30 < y^+ < 300$. A y^+ value close to the lower bound ($y^+ \approx 30$) is most desirable.

- Although FLUENT employs the linear (laminar) law when $y^* < 11.225$, using an excessively fine mesh near the walls should be avoided, because the wall functions cease to be valid in the viscous sublayer.

- As much as possible, the mesh should be made either coarse or fine enough to prevent the wall-adjacent cells from being placed in the buffer layer ($y^+ = 5 \sim 30$).

- The upper bound of the log-layer depends on, among others, pressure gradients and Reynolds number. As the Reynolds number increases, the upper bound tends to also increase. y^+ values that are too large are not desirable, because the wake component becomes substantially large above the log-layer.

- Using excessive stretching in the direction normal to the wall should be avoided.

- It is important to have at least a few cells inside the boundary layer.

Enhanced Wall Treatment: When the enhanced wall treatment is employed with the intention of resolving the laminar sublayer, y^+ at the wall-adjacent cell should be on the order of $y^+ = 1$. However, a higher y^+ is acceptable as long as it is well inside the viscous sublayer ($y^+ < 4$ to 5). There should be at least 10 cells within the viscosity-affected near-wall region ($Re_y < 200$) to be able to resolve the mean velocity and turbulent quantities in that region.

Spalart-Allmaras Models: In summary, for best results with the Spalart-Allmaras model, should be used either a very fine near-wall mesh spacing (on the order of $y^+ = 1$) or a mesh spacing such that $y^+ > 30$.

k-ω Models: Both k-ω models available in FLUENT are available as low-Reynolds-number models as well as high-Reynolds-number models. If the Transitional Flows option is enabled in the Viscous Model panel, low-Reynolds-number variants will be used, and, in that case, mesh guidelines should be the same as for the enhanced wall treatment. However, if this option is not active, then the mesh guidelines should be the same as for the wall functions.

For the conditions of simulation in the present work, the mesh would have to be too coarse in order to obtain y^+ values greater than 30, consequently the results would have no quality. Therefore, the option was to use very refined mesh in order to obtain $y^+ < 5$ and to activate the enhanced wall treatment.

Chapter 6 - Comparison of Viscous Models Results

It is practically impossible to guess which model would be the more appropriate for simulating the flow through a tube array. One could say that the RSM is the more appropriate, because it is the more complete, or that the S-A is actually the most appropriate, because it was developed for aerospace applications, being capable of calculating easily the aerodynamic force. To make the decision easier, the models are put into action. The task chosen for these models was to calculate the case at U_0 = 8,8 [m/s] and y = 4 [mm], so the results can be directly compared to those from the experiment. This specific case was chosen because the velocity is high, making a bit more complicate to model the turbulence, and the tube is considerably displaced, breaking the symmetry, so that the lift calculated may also be compared.

Six turbulent models were tested: RSM, S-A, SST k-ω, k-ε, rk-ε and RNG k-ε. All of the simulations were made using exactly the same mesh, the enhanced wall treatment was activated, the turbulence was always determined at inlet and outlet by the same model: intensity (3%) and hydraulic diameter (0,3 [m]).

The results from those models will be compared quantitatively and qualitatively. Quantitatively by comparison between simulation results for drag and lift acting on the displaced tube and the pressure drop between inflow and outflow in relation to the same results from the experiment. Qualitatively by comparing the pressure profiles generated by each model with the one measured during the experiment.

As the pressure drop measured during the experiment was not made in a very correct way, it is interesting to verify the credibility of the measure by comparing to a calculation

based on empirical data, in this case, the by using the method available by Zukauskas[3], using equation (6.1):

$$\Delta p = f\chi N \frac{\rho U_g^{\ 2}}{2} \tag{6.1}$$

$$U_g = U_0 \frac{P/D}{P/D - 1} \tag{6.2}$$

where Δp in the pressure drop, U_g is the maximum velocity in the array (gap velocity, calculated as function of the pitch ratio – *P/D*), N is the number of rows and f and χ are empirical factors dependent on the Reynolds number and the geometry of the array, they are obtained by interpolating between the lines in the graphs presented by Zukauskas[3]. Considering the difficulties in using the graphs to obtain the coefficients, the prediction from this method is not bad with a deviation of less than 10% when verifying with the experimental measure in Table 6.1.

Table 6.1 Pressure drop, drag and lift for a case at U_0 = 8,8 [m/s] and y = 4 [mm], the deviations are calculated relative to the experimental values.

Model	**Δp**	**Dev. (%)**	**F_D [N/m]**	**Dev. (%)**	**F_L [N/m]**	**Dev. (%)**
Exp.	1057,00	-	8,45	-	-3,53	-
Zukauskas[3]	1144,00	8,23	-	-	-	-
RSM	1055,60	-0,13	8,74	3,47	-4,06	15,15
S-A	909,75	-13,93	7,56	-10,50	-4,09	15,91
SST k-ω	1016,46	-3,84	8,95	5,99	-4,17	18,22
k-ε	1307,13	23,66	13,66	61,77	-0,12	-96,56
rk-ε	1054,72	-0,22	10,59	25,41	-1,07	-69,79
RNG k-ε	794,25	-24,86	7,74	-8,33	-3,02	-14,24

Now analyzing the data in Table 6.1, the pressure drop was calculated very well by the models RSM, SST k-ω and rk-ε, the value calculated by S-A is also acceptable. However, the k-ε calculated a pressure more than 20% higher, and this model is instantly dismissed when verifying that the forces were also very badly estimated, more than 60% for drag and more than 90% for Lift, notice that the lift calculated is almost zero. Taking profit on the situation of bad luck for the k-ε model, the rk-ε may also be dismissed, despite the good calculation of pressure drop, because the forces are very badly estimated, with an error of almost 70% for lift coefficient. The RNG k-ε model had not so bad results, however, because of the bad prediction of pressure drop, the forces showed a tendency to be smaller. The results for force are basically the most important on this work, since they are intended to be used on FEI models.

Finally, of the models that are left, the best results are due to the RSM, followed by the SSTk-ω and the S-A which did not perform so well. These results are pointing to RSM to be the best choice, however, SST k-ω also performed well, and it is much faster for simulating. Talking about time, these simulations were run in a computer with Intel processor Pentium IV at 3Ghz and 1 Gb of RAM, 40 minutes were needed processing and 2500 iterations were realized to achieve desirable convergence. The same case using SST k-ω takes about 20 minutes for achieving desirable convergence.

The experimental results and the results from the simulations vary in different ranges, firstly because the pressure conditions in the experiment are not exactly the same as in the CFD simulations: in the simulation is defined a velocity in the inlet and a zero pressure condition in the outlet, while for the experiment, a wind tunnel of suction was used, so the pressure is zero gauge in the entrance and negative at the exit.

To make a good comparison, the data has to be prepared through a proceeding that is many times applied in the present work: firstly the highest pressure for each profile result has to be found and then subtracted from all the pressure values for each computational and experimental pressure profile, so that the stagnation pressure (that is the highest pressure) is set to be zero, but the original relative profile is preserved. By applying this preceding, the Graphs 6.1 (a) and (b) were plotted, the profiles are separated in two graphs to facilitate viewing.

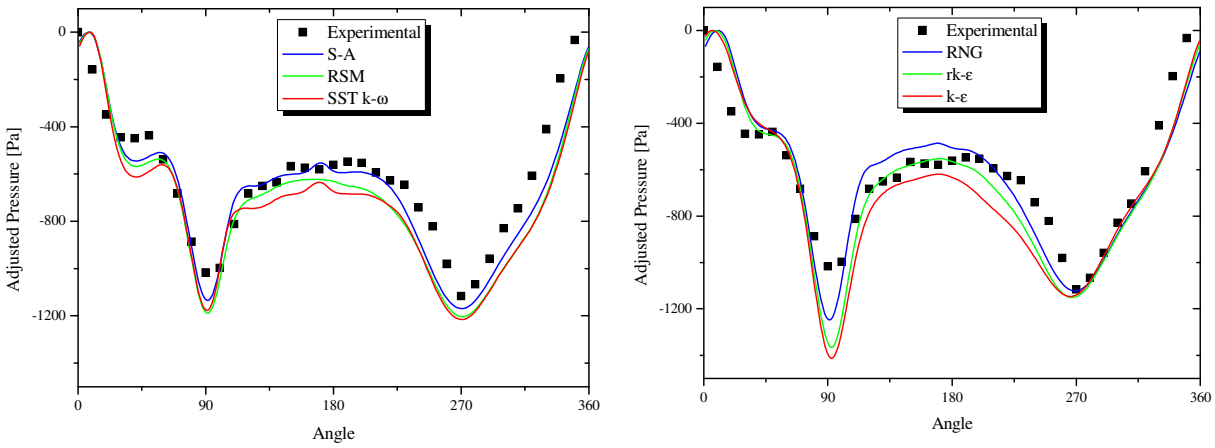

(a) **(b)**

Graphs 6.1 Pressure profiles comparison at U_0 = 8.8 [m/s] and y = 4[mm]

Qualitatively, by observing pressure profiles on Graphs 6.1, between the k-ε models, the RNG version is apparently better adapted to the experimental profile. The RNG was also the best performing between the k-ε models in the quantitative comparison. But anyway, there is no intention for using any k-ε model. Comparing the Graphs 6.1 (a) and (b) one can see that k-ε models have a basic problem at 90°, and the other models fit better at 90°, that is why the force results after integration are better. Between S-A, RSM and SST k-ω, the S-A is better aligned to the experimental results. However, the chosen model believed to be the best one for pursue the research was the RSM.

Chapter 7 - RSM Results and Discussion

7.1 Analysis of the flow

From the results of the simulations, several studies can be made, as for example how does the velocity field changes when the tube is displaced, as can be seen on Figure 7.1. One can observe: how the flow is naturally forced to change its original path as y increases; the fact that the boundary layer is well attached to the tube's wall, presenting just a small detached region in the back of the tube, that is a proper characteristic of a staggered geometry and it is much different of an in-line geometry, where the detachment is quite important; the stagnation point has its position slightly changed downwards as the tube is displaced.

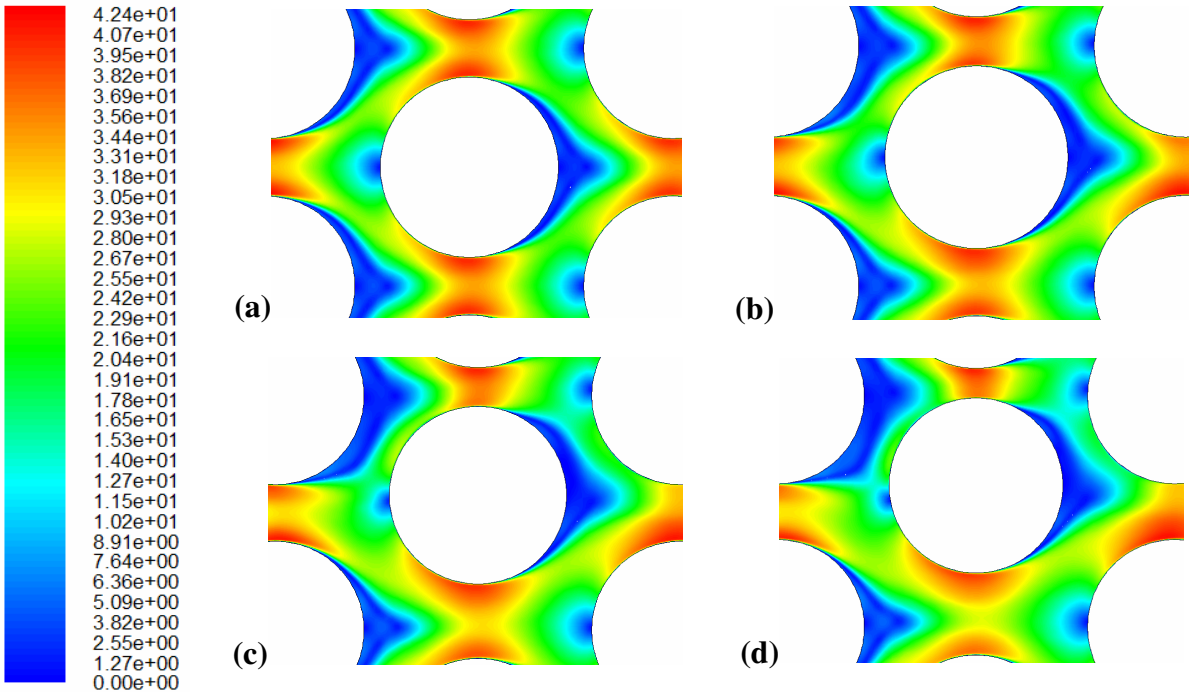

Figure 7.1 Modification on the velocity field as the tube is displaced, U_0 = 8.8 [m/s], y = **(a)** 0, **(b)** 2, **(c)** 4 and **(d)** 6 [mm] (colour scale in [m/s])

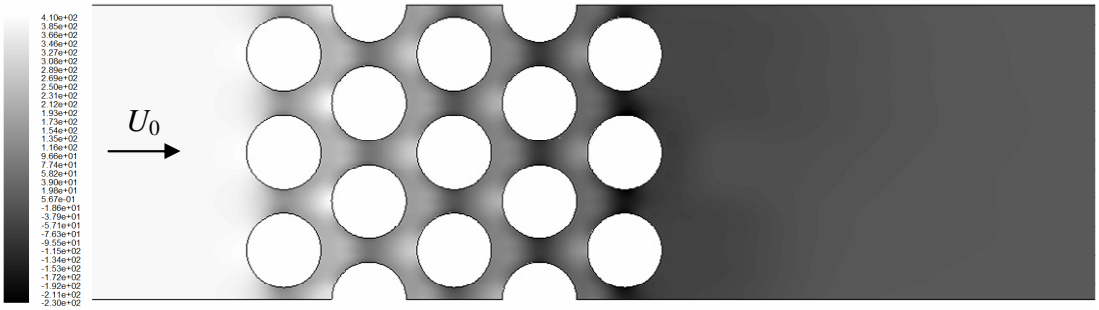

Figure 7.2 Static pressure in [Pa] for a case at U_0 = 5 [m/s] and y = 0 [mm]

The drag force acting on the tubes is almost completely due to the pressure drop through the array, this pressure drop can be verified in Figure 7.2 by checking how the greyscale gets darker at the surface of any tube when moving from in- to out-flow, what means that it decreases.

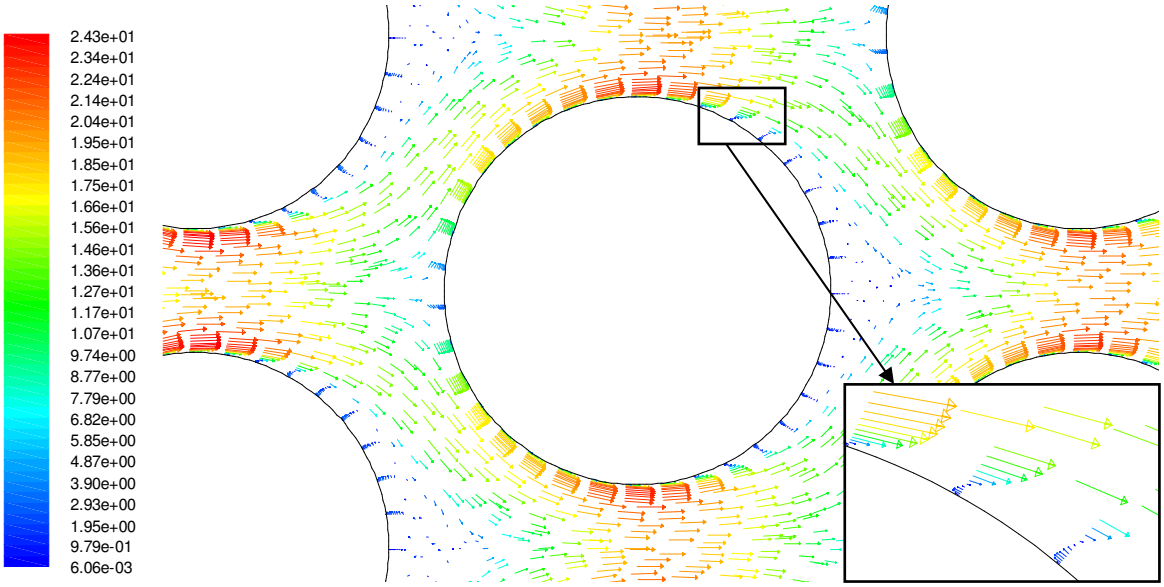

Figure 7.3 Velocity vectors for a case at U_0 = 8,8 [m/s] and y = 0 [mm], in detail the separation of the boundary layer (colour scale in m/s)

On Figure 7.3, the point where boundary layer detachment occurs can be seen in detail. Despite being short, it generates vortices, as can be proved by the velocity vectors suffering an inversion on direction. Vortex generation can be one of the causes of FIV, as it is known, FIV can be caused by more than one mechanism acting at the same time.

7.2 The pressure profiles

From the simulations, the RSM profiles results are extracted and compared to the experimental ones in Graphs 7.1 and 7.2 following.

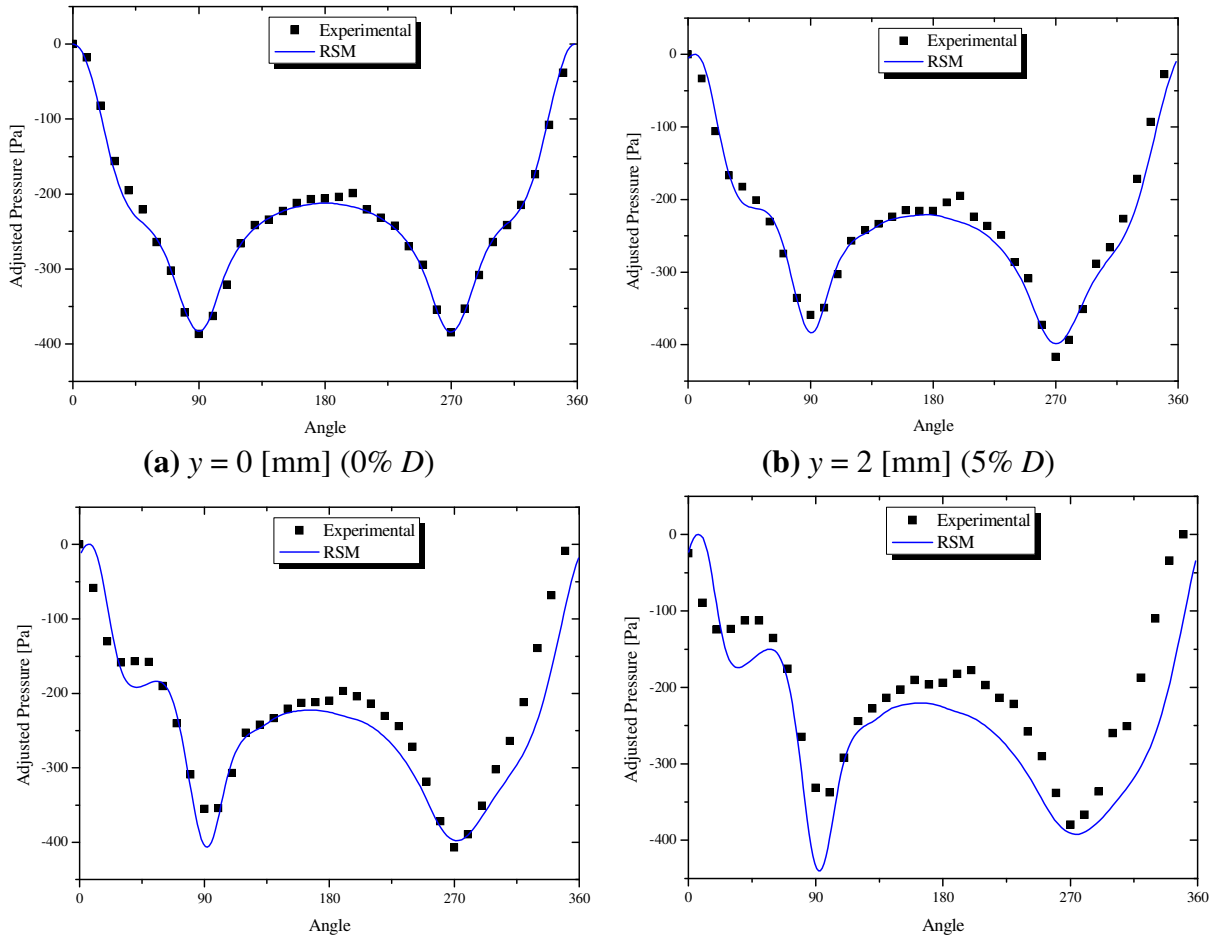

(a) $y = 0$ [mm] (0% D) **(b)** $y = 2$ [mm] (5% D)

(c) $y = 4$ [mm] (10% D) **(d)** $y = 6$ [mm] (15% D)

Graphs 7.1 Pressure profiles comparison at $U_0 = 5$ [m/s]

From Graphs 7.1 and 7.2, one can observe that the pressure profile obtained by simulation matches very well the one measured experimentally for low displacement (0 and 2 [mm]), and as the displacement increases, the affinity between simulation and experimental profiles gets worse.

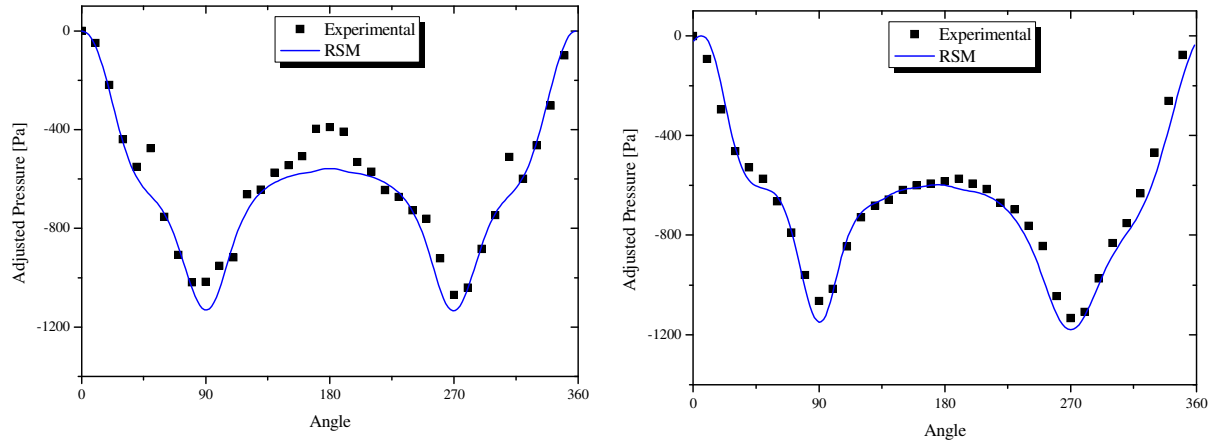

(a) $y = 0$ [mm] (0% D) **(b)** $y = 2$ [mm] (5% D)

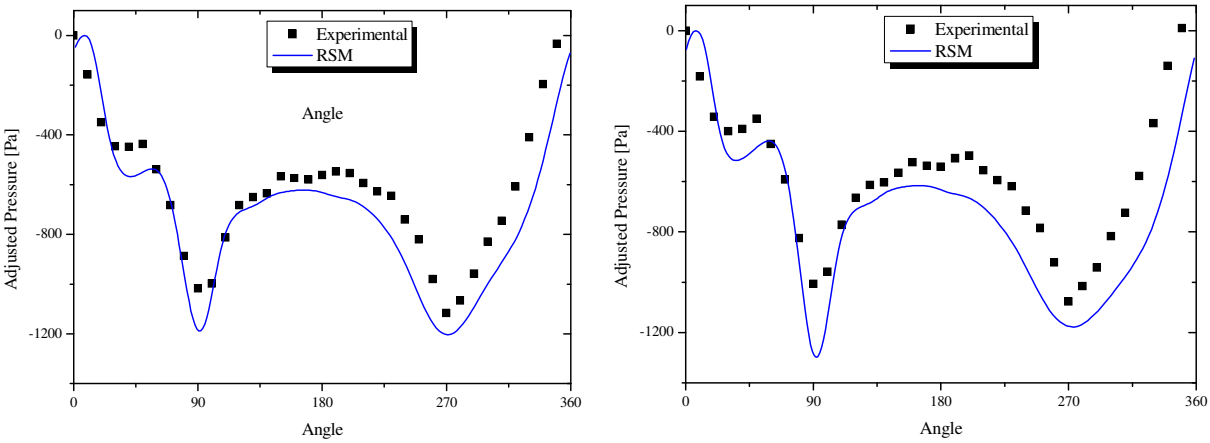

(c) $y = 4$ [mm] (10% D) **(d)** $y = 6$ [mm] (15% D)

Graphs 7.2 Pressure profiles comparison at $U_0 = 8.8$ [m/s]

From those pressure profiles shown in Graphs 7.1 and 7.2, the drags and lifts due to pressure can be calculated. Neglecting viscous effects, as they compose less than 5% of the fluid forces on this cases, the fluid forces calculated from the simulation profiles are compared to those calculated from the experimental profiles (from Table 4.1) on Table 7.1.

Table 7.1 Drags and lifts from the simulations and their deviation from the experimental ones

y [mm]	**U_0 = 5 [m/s]**				**U_0 = 8,8 [m/s]**			
	F_D [N/m]	**Dev. (%)**	**F_L [N/m]**	**Dev. (%)**	**F_D [N/m]**	**Dev. (%)**	**F_L [N/m]**	**Dev. (%)**
0	3,30	7,9	-0,03	-	8,52	39,8	-0,07	-
2	3,39	10,3	-0,94	-22,0	8,76	3,7	-2,54	-3,3
4	3,38	0,8	-1,04	-28,9	8,74	3,5	-4,06	15,2
6	3,56	4,4	-0,89	-47,0	9,07	7,2	-3,31	-15,8

From Table 7.1 some effects can be verified:

- The simulations can predict the drag much better than the lift.

- The simulation predicts that the lift increases as *y* is increased from 0 to 2 and 4 [mm], but it decreases from 4 to 6 [mm], what is incoherent with the experimental result. This is explained by the prediction of pressure in the lower part of the

- These results are considerably better than the results obtained from the very first simulations made in the beginning of this work, with a mesh of bad quality, those even obtained deviations of more than 200%, while for these new simulations the worse deviation is no more than 50%.

7.3 Neighbour tubes

An advantage of computational simulation is the fact that data is calculated for everything, and one can, for example, know the force acting in any of the other tubes in the array. The interest in this section is to discuss specifically the influence of the displacement of the principal tube on the forces that arise at the neighbour tubes, these are plotted on Graphs 7.3 and 7.4 following.

It can be seen that for both inlet velocities, the Drags and Lifts vary in the same way. At zero position, the drag is about 9 [N] for every tube. As the principal tube is displaced, the pressure field is modified, so that the drag force on tubes 2, 6 and 3 is increased, while for tubes 1, 5 and 4 the opposite occurs, and their drag force is decreased, however the variation of drag on tubes 3 and 4 is not as significant as for the others. Notice that the drag for the principal tube itself varies less significantly than for all other tubes. Now, referring about the lift force, the lift is practically null when the case is symmetric (y = 0 [mm]), but when the

principal tube is displaced, the lift force on the neighbour tubes vary in a way not as trivial as the drag does, it can increase and then decrease, as it does significantly for tube 3. The lift for tube 2 is quite interesting, cause it gets to be even higher than the lift for the principal tube at the nearer position (y = 6 [mm]).

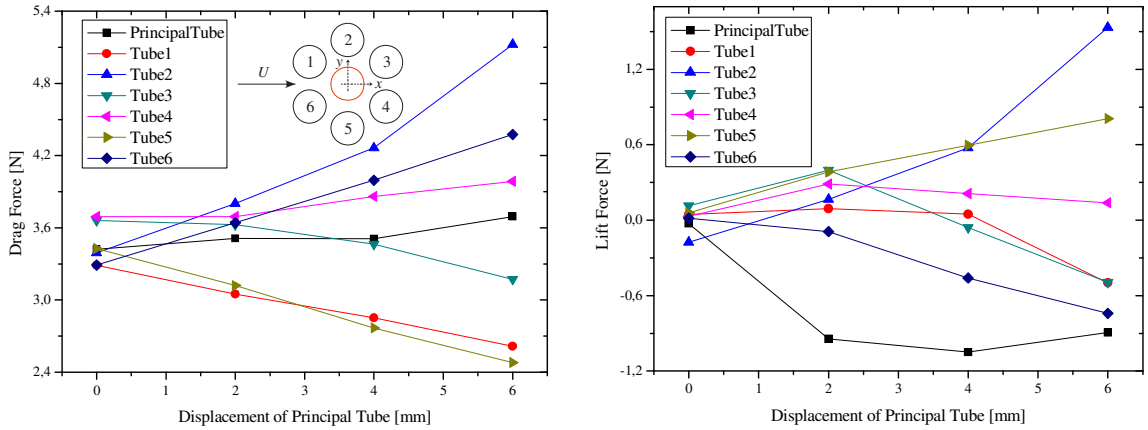

Graphs 7.3 Drag and Lift as a function of the principal tube's displacement (y) for the neighbouring tubes for U_0 = 8,8 [m/s]

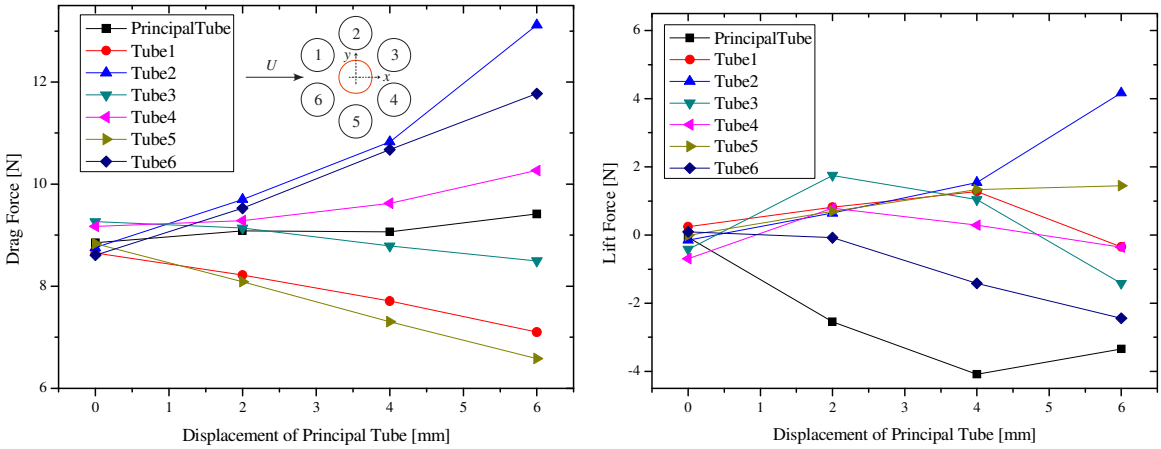

Graphs 7.4 Drag and Lift as a function of the principal tube's displacement (y) for the neighbouring tubes for U_0 = 8,8 [m/s]

This analysis of the forces shows how the tubes in a bundle subject to cross flow can be closely related and the displacement of one tube could provoke the other tubes to move or deform due to the fluid forces.

8 Conclusions and Future Work

Concluding this work, some points must be highlighted:

- CFD is a powerful tool for studying flows through tube arrays and can be used to predict the forces arising to the tubes;
- The RSM viscous model is more realistic and provides better results when comparing to the other RANS models available on FLUENT;
- The drag forces calculated by FLUENT are more exact than the lift forces for a staggered normal triangular tube array;
- As important as the choice of viscous model is the mesh design, especially the cell size in the near wall region, the improvement on the mesh proved to reduce substantially the error on the calculations of fluid forces.

For a future work, it would be very interesting to develop an unsteady simulation using dynamic mesh, this way it might be possible to reproduce the experiments used for determination of FEI parameters.

Apart of the idea of an unsteady model, it would be also interesting to work on a method for bringing together the results from steady simulations and the quasi-steady fluidelastic instability models.

A paper was published and presented at the Joint Conference of the Association for Computational Mechanics in Engineering (ACME - UK) and the Irish Society for Scientific and Engineering Computation (ISSEC) in Belfast, 2006, presenting some of the results and advances of the present work[24].

References

[1] WIKIPEDIA, The Free Encyclopedia (2006), **Tacoma Narrows Bridge**. Article in the world Wide Web, accessed in 16 May 2006, available at <http://en.wikipedia.org/wiki/Tacoma_Narrows_Bridge>

[2] PAIDOUSSIS, M. (1981). **Fluidelastic vibration of cylinder arrays in axial and cross flow: state of the art**. Journal of Sound and Vibration 76(3), 329--360.

[3] ZUKAUSKAS, A.; ULINSKAS R.; KATINAS, V., (1988), **Fluid Dynamics and Flow-Induced Vibrations of Tube Banks**. Experimental and applied heat transfer guide books. Hemisphere Publishing Corporation.

[4] ROBERTS, B. W. (1962), **Low Frequency Self-Excited Vibration in a Row of Circular Cylinders Mounted in an Airstream**. Ph.D. thesis, University of Cambridge, Cambridge, UK.

[5] CONNORS, H. J. (1970), **Fluidelastic Vibration of Tube Arrays Exited by Cross Flow**. Flow Induced Vibrations in Heat Exchangers, ed. D. D. Reiff, ASME, New York, NY, pp. 42-56.

[6] PRICE, S. J. (2001), **An investigation on the Use of Connors' Equation to Predict Fluidelastic Instability in Tube Arrays**. Transactions of the ASME, vol. 123, November 2001.

[7] MESKELL, C. (2005), **On the Underlying Fluid Mechanics Responsible for Damping Controlled Fluidelastic Instability in Tube Arrays**. Procedures of

PVP2005: ASME Pressure Vessels and Piping Division Conference, Denver, Colorado, USA, July 17-21, 2005.

[8] PAIDOUSSIS, M. P.; PRICE, S. J. (1988), **The Mechanisms Underlying Flow-Induced Instabilities of Cylinder Arrays in Cross Flow**. Journal of Fluid Mechanics vol. 187, pp. 45-59.

[9] PRICE, S. J.; PAIDOUSSIS, M. P. (1984), **An Improved Mathematical Model for the Stability of Cylinder Rows Subject to Cross-Flow**. Journal of Sound and Vibration, 97(4), 615-640.

[10] GRANGER, S.; PAIDOUSSIS M. P. (1996), **An Improvement to the Quasi-Steady Model With Application to Cross-Flow-Induced Vibration of Tube Arrays**. Journal of Fluid Mechanics, 320, 163-184.

[11] MESKELL, C (2004), **Numerical Estimation of Fluid Force Coefficients in a Normal Triangular Tube Array**. Ecole Polytechnique, Paris, 6-9th July 2004.

[12] FLUENT INC. (2003), **User's Guide**. FLUENT 6.1 Documentation, HTML and PDF versions.

[13] SPALART, P.; ALLMARAS, S (1992), **A one-equation turbulence model for aerodynamic flows**. Technical Report AIAA-92-0439, American Institute of Aeronautics and Astronautics, 1992.

[14] LAUNDER, B. E.; SPALDING, D. B. (1972), **Lectures in Mathematical Models of Turbulence**. Academic Press, London, England, 1972.

[15] YAKHOT, V.; ORSZAG, S. A. **Renormalization Group Analysis of Turbulence: I. Basic Theory**. Journal of Scientific Computing, 1(1):1-51, 1986.

[16] SHIH, T.-H.; LIOU, W. W.; SHABBIR, A.; YANG, Z.; ZHU, J. **A New k-ε Eddy-Viscosity Model for High Reynolds Number Turbulent Flows - Model Development and Validation**. Computers Fluids, 24(3):227-238, 1995.

[17] CHOUDHURY, D. **Introduction to the Renormalization Group Method and Turbulence Modeling**. Fluent Inc. Technical Memorandum TM-107, 1993.

[18] WILCOX, D. C. **Turbulence Modeling for CFD**. DCW Industries, Inc., La Canada, California, 1998.

[19] MENTER, F. R. **Two-Equation Eddy-Viscosity Turbulence Models for Engineering Applications**. AIAA Journal, 32(8):1598-1605, August 1994.

[20] GIBSON, M. M. LAUNDER, B. E. **Ground Effects on Pressure Fluctuations in the Atmospheric Boundary Layer**. J. Fluid Mech., 86:491-511, 1978.

[21] LAUNDER, B. E. **Second-Moment Closure: Present... and Future?** Inter. J. Heat Fluid Flow, 10(4):282-300, 1989.

[22] LAUNDER, B. E.; REECE, G. J.; RODI; W. **Progress in the Development of a Reynolds-Stress Turbulence Closure**. J. Fluid Mech., 68(3):537-566, April 1975.

[23] SCHRODER, K.; GELBE, H. (1999), **Two- and three-dimensional CFD-simulation of flow-induced vibration excitation in tube bundles**. Chemical Engineering and Processing, Volume 38, Issues 4-6, September 1999, Pages 621-629.

[24] SANCHES, R. A. K.; MESKELL, C. (2006), **Numerical Evaluation of Force Coefficients for Analysis of Flow Induced Vibrations in Tube Arrays**. Proceedings of a Joint Conference of the ACME (UK) and ISSEC, 19th-20th April 2006, Queen's University, Belfast.

[25] MESKELL, C. (1999), **Identification of a non-linear model for Fluidelastic instability in a normal triangular tube array**. A thesis submitted to the University of Dublin for the degree of Ph.D. Department of Mechanical and Manufacturing Engineering, Trinity College, Dublin 2, Ireland. May, 1999.

Appendix 1 - Experiment Details

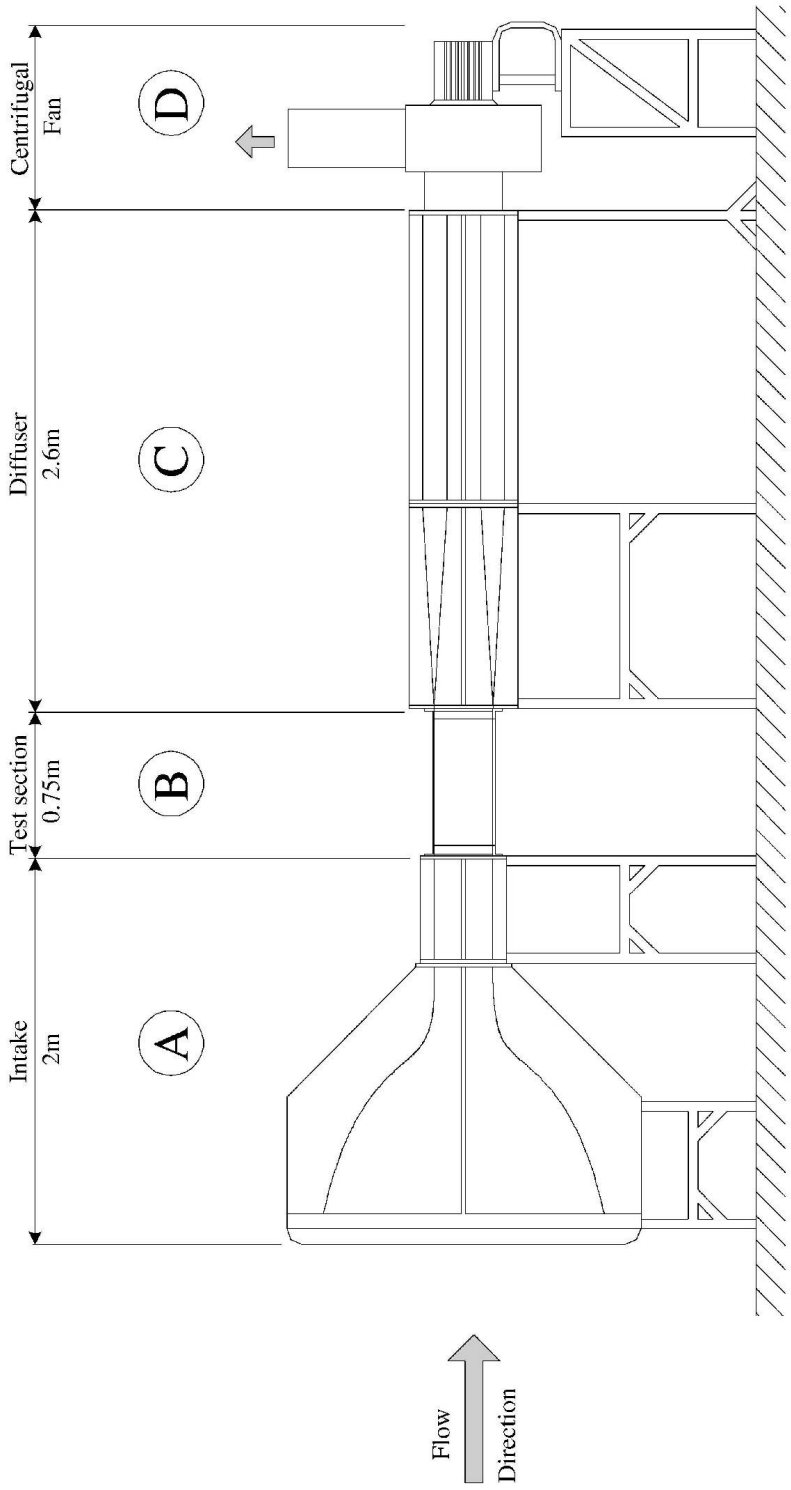

Figure A1.1 Sketch of the wind tunnel extracted from Meskell[25]

Figures A1.2 Details on the assembly of the tube used for measuring the pressure profiles

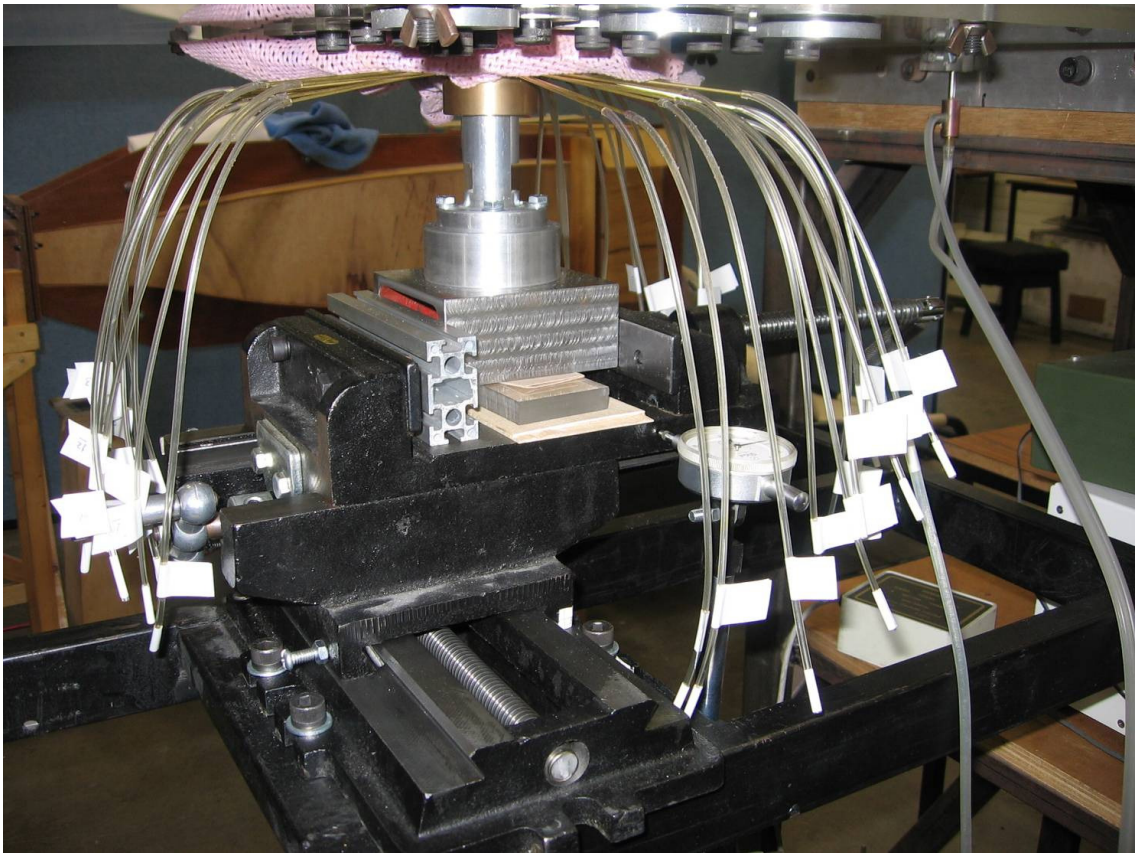

Figure A1.3 Detail on the positioning system of the principal tube

Appendix 2 - Experimental Data

Table A2.1 Experiment data for U_0 = 5 [m/s]

Angle (°)	**Pressure in Pascal for displacement *y*=**			
	0 [mm]	**2 [mm]**	**4 [mm]**	**6 [mm]**
0	-83,385	-83,385	-90,252	-133,416
10	-101,043	-116,739	-149,112	-198,162
20	-165,789	-189,333	-220,725	-233,478
30	-239,364	-250,155	-249,174	-232,497
40	-278,604	-265,851	-247,212	-221,706
50	-304,11	-284,49	-248,193	-221,706
60	-347,274	-313,92	-280,566	-244,269
70	-385,533	-358,065	-330,597	-284,49
80	-441,45	-418,887	-399,267	-373,761
90	-469,899	-442,431	-445,374	-440,469
100	-446,355	-432,621	-444,393	-446,355
110	-404,172	-386,514	-397,305	-401,229
120	-349,236	-340,407	-343,35	-353,16
130	-324,711	-325,692	-332,559	-336,483
140	-317,844	-316,863	-323,73	-322,749
150	-306,072	-307,053	-310,977	-311,958
160	-295,281	-298,224	-303,129	-299,205
170	-290,376	-299,205	-302,148	-305,091
180	-289,395	-299,205	-300,186	-303,129
190	-287,433	-287,433	-287,433	-291,357
200	-282,528	-278,604	-294,3	-286,452
210	-304,11	-307,053	-304,11	-306,072
220	-314,901	-319,806	-320,787	-322,749
230	-325,692	-332,559	-334,521	-330,597
240	-353,16	-369,837	-361,989	-366,894
250	-377,685	-392,4	-409,077	-399,267
260	-437,526	-456,165	-462,051	-447,336
270	-467,937	-500,31	-497,367	-488,538
280	-436,545	-476,766	-479,709	-475,785
290	-391,419	-434,583	-441,45	-445,374
300	-347,274	-371,799	-392,4	-368,856
310	-324,711	-349,236	-354,141	-360,027
320	-298,224	-309,996	-302,148	-296,262
330	-257,022	-255,06	-229,554	-218,763
340	-191,295	-176,58	-158,922	-143,226
350	-121,644	-110,853	-99,081	-108,891

Table A2.2 Experiment data for U_0 = 8,8 [m/s]

Angle (°)	**Pressure in Pascal for displacement *y*=**			
	0 [mm]	**2 [mm]**	**4 [mm]**	**6 [mm]**
0	-239,364	-240,345	-255,06	-297,243
10	-288,414	-333,54	-412,02	-478,728
20	-459,108	-534,645	-603,315	-639,612
30	-678,852	-703,377	-700,434	-696,51
40	-790,686	-768,123	-703,377	-687,681
50	-716,13	-815,211	-691,605	-647,46
60	-992,772	-905,463	-793,629	-747,522
70	-1147,77	-1031,03	-937,836	-889,767
80	-1258,62	-1200,74	-1141,88	-1122,26
90	-1255,68	-1304,73	-1272,36	-1304,73
100	-1191,92	-1255,68	-1252,74	-1255,68
110	-1157,58	-1085,97	-1067,33	-1069,29
120	-902,52	-968,247	-937,836	-961,38
130	-882,9	-922,14	-905,463	-910,368
140	-814,23	-898,596	-889,767	-900,558
150	-784,8	-858,375	-822,078	-862,299
160	-748,503	-840,717	-828,945	-820,116
170	-635,688	-833,85	-834,831	-834,831
180	-629,802	-824,04	-816,192	-837,774
190	-647,46	-814,23	-802,458	-804,42
200	-771,066	-833,85	-808,344	-794,61
210	-810,306	-855,432	-848,565	-852,489
220	-884,862	-911,349	-882,9	-891,729
230	-912,33	-936,855	-900,558	-915,273
240	-966,285	-1003,56	-995,715	-1012,39
250	-1000,62	-1084,01	-1076,16	-1082,04
260	-1162,49	-1285,11	-1235,08	-1219,38
270	-1308,65	-1373,4	-1371,44	-1373,4
280	-1280,21	-1348,88	-1321,41	-1312,58
290	-1123,25	-1214,48	-1213,5	-1239
300	-986,886	-1072,23	-1084,01	-1114,42
310	-750,465	-992,772	-1000,62	-1021,22
320	-838,755	-873,09	-862,299	-875,052
330	-703,377	-709,263	-665,118	-665,118
340	-542,493	-502,272	-451,26	-437,526
350	-339,426	-316,863	-288,414	-286,452